Study of Structural Imperfections in Natural Type I Diamonds by High-Resolution X-ray Diffraction Techniques

R. R. Ramanan, S. Niranjana N. Goswami and Krishan Lal*

National Physical Laboratory, New Delhi 110 012, India. E-mail: klal@csnpl.ren.nic.in

Abstract

Results of characterization of defects in natural diamond crystals by high-resolution X-ray diffractometry, absolute integrated intensity (ρ) measurements, topography and diffuse X-ray scattering (DXS) techniques are reported. The samples are $\langle 111 \rangle$ natural diamond platelets of dimensions ~2 × 2 mm with thickness in the range ~0.5–1 mm. A five-crystal X-ray diffractometer in three-crystal configuration as well as a four-crystal diffractometer were employed with Mo $K\alpha_1$ as the exploring radiation. Infrared absorption measurements showed that the samples belong to type Ia variety and contained varying concentrations of A and B forms of nitrogen aggregates as well as platelets. There were large variations in the values of diffraction curve half-widths (18 to 550″) and values of ρ (2.4 × 10^{-5}–76 × 10^{-5} rad) for 111 reflection, showing a wide variation in crystalline perfection. Projection and composite stationary X-ray topographs recorded with different diffraction vectors showed the presence of defects like low-angle boundaries. From the analysis of the observed distribution of diffuse X-ray scattering (DXS), point defect clusters were characterized. The clusters were of interstitial as well as vacancy type. The sizes of the defect clusters (R_{cl}) were determined to be in the range 40 to 190 nm and the volumes of the defect clusters (A_{cl}) were in the range ~1 × 10^{-25}–28 × 10^{-25} m^3. The defect clusters with sizes reported here could be investigated as the measurements were made close to the reciprocal-lattice points. The platelet size was found to vary inversely with the total concentration of nitrogen.

1. Introduction

Diamond crystals have immense scientific and technological importance in view of their excellent physical properties like extreme hardness, wide bandgap and high thermal conductivity. All diamonds give characteristic infrared absorption between ~4 and 6 μm. Nitrogen is the major impurity in diamond, due to which infrared absorption bands in the 7–8.5 μm range are observed. The role of nitrogen in diamond has been thoroughly investigated (Field, 1992). Depending on the presence or absence of appreciable concentration of nitrogen as indicated by the infrared absorption near 7.8 μm, diamonds have been classified into type I and type II varieties. In type I diamonds, nitrogen may exist in various forms, namely A defects, B defects or complex platelets (Walker, 1979).

Since the early thirties, extensive research work has been carried out on lattice imperfections in natural diamond crystals by using a variety of spectroscopic, X-ray diffraction and other physical measurement techniques (Davies, 1984; Field, 1992). These efforts were aimed at understanding the effect of crystal defects on physical properties and their role in the growth processes. Recently, advanced techniques like high-resolution transmission electron microscopy (HRTEM) (Barry *et al.*, 1987), high-resolution X-ray diffraction (Lal *et al.*, 1990, 1995) and Fourier transform infrared (FTIR) spectrometry (Kiflawi *et al.*, 1994) have also been widely employed to characterize a variety of defects like boundaries, growth bands, platelets, voidites and clustering of impurities. However, no systematic detailed investigation on imperfections like point defects and their clusters in diamond crystals has been carried out. In recent years, the high-resolution diffuse X-ray scattering (DXS) technique has been shown to be successful in the characterization of point defects and their clusters (Dederichs, 1973; Holy & Kubena, 1992; Lal, 1989; Lal & Bhagavannarayana, 1989; Ramanan *et al.*, 1995; Ramanan & Lal, 1996). We have carried out a detailed investigation on the characterization of defects including point defects and their aggregates in natural diamond crystals of varying degree of perfection by high-resolution X-ray diffractometry, absolute integrated intensity measurements, topography and diffuse X-ray scattering techniques. The gross structural perfection of the samples was evaluated by using diffractometry, experimentally determined absolute values of integrated intensities and traverse and stationary X-ray topography. FTIR spectra have been recorded to obtain information about the state of nitrogen clustering. An attempt has also been made to correlate these results with point defect cluster parameters obtained from the DXS measurements. Results of this study are reported here.

2. Experimental details

2.1. Specimen crystals

The samples were broadly triangular shaped (approximately 2 × 2 mm) unpolished platelets of natural diamond crystals. Their thicknesses were in the range ~0.5–1.1 mm. The larger surfaces of the crystals were parallel to (111) planes.

2.2. High-resolution X-ray diffraction experiments

Two multicrystal X-ray diffractometers designed and developed at NPL by Lal and co-workers were employed in this investigation. A five-crystal X-ray diffractometer was employed in a three-crystal configuration for high-resolution diffractometry, absolute integrated intensity (ρ) measurements and high-resolution X-ray diffraction topography (Lal, 1993). The other diffractometer was a four-crystal system specially designed for high-resolution diffuse X-ray scattering (DXS) measurements, X-ray diffractometry and determination of ρ (Lal & Bhaga-vannarayana, 1989). Schematic line diagrams of the two diffractometers are shown in Figs. 1(a) and (b). In both cases, the X-ray beam emerging from a fine-focus sealed tube is collimated by a long collimator fitted with a fine slit. This beam is diffracted from a pair of (111) silicon monochromator crystals of Bonse–Hart type (Bonse & Hart, 1965), which are set in (+, −) geometry. The $K\alpha_1$ and $K\alpha_2$ components of the $K\alpha$ characteristic line are well resolved and the $K\alpha_1$ beam is isolated with the help of a fine slit as shown in Figs. 1(a) and (b). High-resolution X-ray diffractometry and topography experiments were performed with (+, −, +) configuration of the diffractometer with the specimen in Laue geometry. Experiments were performed with ($\bar{2}20$) and ($02\bar{2}$) diffraction planes in the symmetrical Laue geometry and ($\bar{1}11$) planes in the asymmetrical Laue geometry. For recording diffraction curves, the specimens were rotated at an angular interval of ~1″ and the intensity at each point was measured by a scintillation counter (M/s Bicron Corp., Model P-12, USA) and counting system
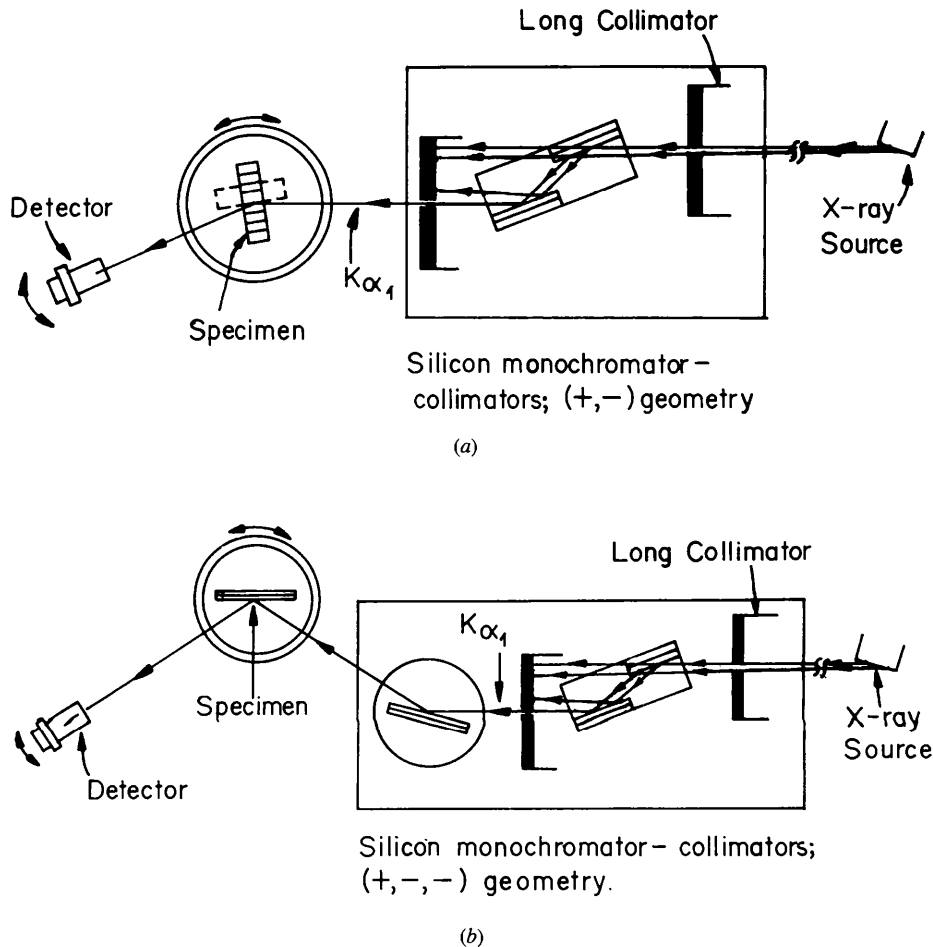

(a)

(b)

Fig. 1. (a) A schematic line diagram of the five-crystal X-ray diffractometer used in the three-crystal configuration which was developed at NPL. (b) A schematic line diagram of the four-crystal X-ray diffractometer developed at NPL.

(M/s Canberra Industries Inc., USA). Typical counting times were 20 s at each point.

In the multicrystal diffractometer of Fig. 1(b), all the components up to the Bonse–Hart monochromator crystals are identical to those in the diffractometer of Fig. 1(a). The $K\alpha_1$ beam obtained after two diffractions is further monochromated and collimated by a diffraction from a (111) silicon crystal in $(+, -, -)$ geometry. The exploring beam has a high spectral purity $(\Delta\lambda/\lambda \sim<10^{-5})$ as expected. The divergence in the horizontal plane (plane of diffraction) was estimated to be $\ll 3''$. The specimen forms the fourth crystal stage of the diffractometer, which is mounted on a turntable that can be rotated at an angular interval of $1''$ about the vertical axis. The width of the exploring beam was maintained at ~0.2 mm in the plane of diffraction and its height was ~1 mm. DXS measurements were performed along two mutually perpendicular directions in reciprocal space, namely $\pm[111]$ and $\pm[110]$ around the 111 reciprocal-lattice point (RLP). The diffuse X-ray scattering intensity was measured using a scintillation counter indigenously developed at NPL connected to a Philips microprocessor-controlled counting system (PW 1710). At low values of diffusely scattered intensity, long time intervals of the order of 500 s were employed to achieve a good signal-to-noise ratio. Mo $K\alpha_1$ was the exploring radiation in all the experiments.

2.3. FTIR measurements

Infrared measurements have been made in the wavelength range 2.5–25 μm at room temperature (300 K). A Nicholet (model 510 P) FTIR spectrophotometer was employed. The crystals were cleaned and mounted in a special sample holder. The beam was 1.5 mm in diameter and the specimen was positioned carefully to ensure that all the radiation passed through the sample before reaching the detector. The number of scans was optimized to 100 to achieve good signal-to-noise ratio and the resolution was fixed at 4 cm^{-1}.

3. Results and discussion

3.1. FTIR measurements

Fig. 2 shows a typical FTIR spectrum of one of the samples (labelled 1). For the sake of clarity, the spectrum in the range 4–14 μm is shown here. In this figure, we can see typical absorption bands of diamond between 4 and 6 μm in addition to a sharp absorption band at 7.3 μm (P) and two broad bands near 7.8 μm (Q) and 8.5 μm (R). Platelet defects are known to be responsible for the 7.3 μm sharp band. Further, the bands at 7.8 and 8.5 μm have been attributed to A and B clusters of nitrogen (Walker, 1979). The presence of the bands P, Q and R show that this crystal belongs to type Ia variety (Walker, 1979). Similar FTIR spectra were obtained with other diamonds studied in this investigation. These were

Table 1. *Values of infrared absorption coefficient due to A (μ_A), B (μ_B) and platelet (μ_p) defects and concentration of nitrogen in A (N_A) and B (N_B) forms of nitrogen aggregates in the diamond samples*

Sample	μ_A (cm^{-1})	μ_B (cm^{-1})	μ_p (cm^{-1})	N_A (at. in 10^6)	N_B (at. in 10^6)
No. 1	20.1	5.0	22.3	351	519
No. 3	5.4	0.9	0.3	95	97
No. 4	1.0	2.2	2.4	17	225
No. 7	34.7	0.8	2.8	607	85
No. 13	3.5	1.3	1.4	61	141

similar to the spectrum shown in Fig. 2 but the strength of absorption at bands P, Q and R varied from sample to sample. From the experimentally determined coefficient of absorption, μ (in cm^{-1}) at 7.8 and 8.5 μm, and the empirical relations given by Davies (1981) and Woods *et al.*, 1990), one can determine the concentration of nitrogen (in atoms in 10^6) in A and B forms of nitrogen impurity. This relation is (Woods *et al.*, 1990)

$$N_A = 17.5\mu_A \quad \text{and} \quad N_B = 103\mu_B, \qquad (1)$$

where, μ_A and μ_B are the absorption coefficients at 7.8 μm due to A and B forms and N_A and N_B are the concentrations of nitrogen in A and B forms, respectively. Table 1 shows the values of coefficients of absorption due to platelets (μ_p), the A defect form (μ_A) and the B defect form (μ_B) determined from the experimental data obtained with five different crystals and the values N_A and N_B determined using (1). It can be seen that the specimen crystals have varying concentrations of platelets and nitrogen in A and B forms.

3.2. Evaluation of degree of perfection of diamond specimens by high-resolution X-ray diffractometry, absolute integrated intensity (ρ) measurements and X-ray diffraction topography experiments

Fig. 3 shows a typical diffraction curve recorded with specimen 13 in $(+, -, -, +)$ configuration of the
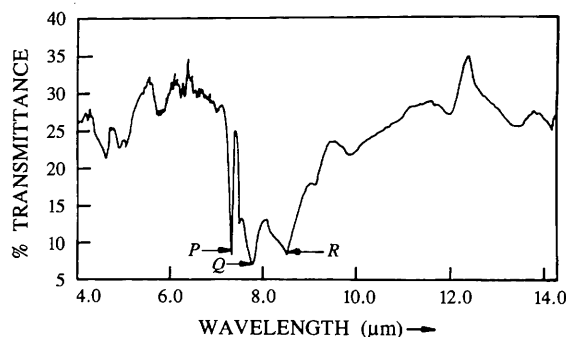

Fig. 2. A typical FTIR absorption spectrum of a diamond specimen crystal (No. 1).

multicrystal X-ray diffractometer. (111) diffracting planes in symmetrical Bragg geometry and Mo $K\alpha_1$ exploring radiation were used. The diffraction curve is quite sharp with a half-width ~18″. The theoretical value of the half-width of the diffraction curve for (111) planes under present experimental conditions, calculated using the plane-wave dynamical theory is 1.96″ (Lal et al., 1990). In the experimental curve, a slight broadening is expected due to dispersion arising out of difference in the lattice parameters of the monochromator crystals [(111) silicon] and the specimen crystal [(111) diamond]. However, the use of the (+, −, −) setting, i.e. dispersive setting of the third monochromator crystal, has improved the spectral purity of $K\alpha_1$ radiation and, as the $\Delta\lambda/\lambda$ is less than 10^{-5}, the broadening due to lattice mismatch is quite negligible. Hence, one can conclude that the observed difference between the theoretical and experimental half-widths is predominantly due to the structural imperfections in the specimen.

It is well known that, in addition to the magnitude of the diffraction curve half-width, the magnitude of the absolute integrated intensity (ρ) is also a good measure of crystalline perfection. From the ratio of the area under the experimentally obtained diffraction curve to the incident intensity (I_o), one can obtain the absolute value of ρ. The intensity of the exploring beam was carefully measured and maintained constant throughout the experiment. In the case of specimen 13 (Fig. 3), the experimental value of ρ was determined as 2.5×10^{-5} rad. This was compared with the theoretical values calculated for an ideally perfect diamond crystal as well as for an ideally mosaic crystal (James, 1950). For an ideally perfect crystal, ρ is

given by (James, 1950)

$$\rho = (8/3\pi)N\lambda^2|F|(e^2/mc^2)[(1 + |\cos 2\theta|)/2 \sin 2\theta],$$

(2)

where N is the number of unit cells per unit volume of the crystal, λ is the wavelength of the exploring radiation, F is the structure factor for the reflection under consideration, e and m are the charge and mass of the electron, c is the velocity of light and θ the Bragg angle. For an ideally imperfect or mosaic crystal, ρ is given by the relation (James, 1950)

$$\rho = (N^2\lambda^3/2\mu)|F|^2(e^2/mc^2)^2[(1 + \cos^2 2\theta)/2 \sin 2\theta],$$

(3)

where μ is the absorption coefficient and all the other notations represent the same parameters as in (2) above.

For (111) diffracting planes of diamond and Mo $K\alpha_1$ radiation as the exploring beam, the theoretical value of ρ for ideally perfect and imperfect crystals were calculated as 1.2×10^{-5} and 245.5×10^{-5} rad, respectively. It can be seen that the experimental value of ρ (2.5×10^{-5} rad) is close to the theoretical value for a perfect rather than an imperfect crystal. This result is in agreement with that obtained by using X-ray diffractometry.

Diffraction curves were also recorded with all the other specimens. These varied widely in shape as well as in the values of the half-widths and ρ. The half-widths were in the range 20 to 550″ and the ρ values were in the range 4.7×10^{-5} to 76.7×10^{-5} rad. Diffraction curves of some of the crystals consisted of more than one well resolved peak, showing the presence of subgrain
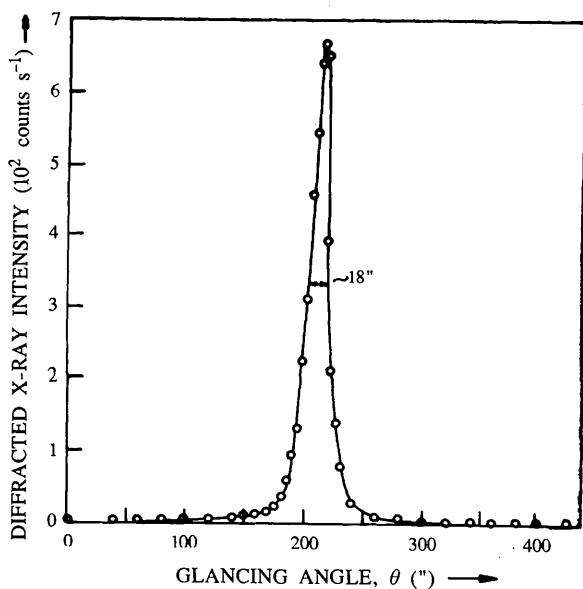

Fig. 3. A typical diffraction curve of a (111) diamond specimen (No. 13). Mo $K\alpha_1$ radiation, (+, −, −, +) configuration of the diffractometer and symmetrical Bragg geometry were used.
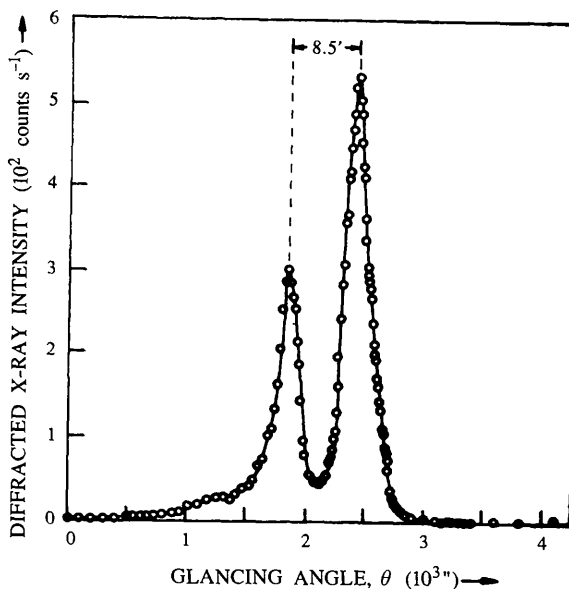

Fig. 4. A typical diffraction curve of a (111) diamond specimen (No. 9) showing the presence of a low-angle boundary. Experimental details are as in Fig. 3.

boundaries. Fig. 4 shows a typical diffraction curve for one such specimen (No. 9). In this case, one can see two well resolved diffraction peaks showing the presence of a subgrain boundary with an angle ~8.5' between subgrains.

From the X-ray diffractometry experiments, it was found that specimen 13 (Fig. 3) has the highest degree of perfection amongst all the crystals. Therefore, additional experiments were performed on this specimen in Laue geometry with the $(+, -, +)$ configuration of the diffractometer. Diffraction curves were recorded with $\bar{2}20$ and $02\bar{2}$ symmetric reflections and $\bar{1}11$ asymmetric reflection from different regions of the specimen. It was found that there was a variation in the values of half-width and ρ from region to region. Except for a small region where the half-width was ~10″, the values of the half-width varied from 18 to 32″ and values of ρ varied from 0.7×10^{-5} to 1.6×10^{-5} rad, in comparison with the value of ρ_{220} (0.2×10^{-5} rad) for a perfect diamond crystal.

Fig. 5 shows a typical traverse topograph of specimen 13 recorded in the $(+, -, +)$ configuration of the diffractometer. The specimen was oriented for diffraction from the $(\bar{2}20)$ planes in symmetrical Laue geometry. In this topograph, the dominant feature is the strong black line, making an angle of ~60° with the diffraction vector **g**. To improve the sensitivity of the topography experiments, a set of stationary topographs was also recorded. The topographs were recorded one after the other on the same film by translating the film and crystal across the X-ray beam after each exposure. The linear movement was equal to the width of the stationary topograph and therefore the composite topograph covers the entire volume of the crystal. Fig. 6 shows a typical set of such topographs recorded for the specimen of Fig. 5. The

details in this figure are far more clear than those of Fig. 5, as expected. The dominant feature is again the black band running at ~60° to the diffraction vector. For detailed investigation of the nature of this band-like feature, projection and stationary topographs were recorded with other diffracting planes. It was found that this feature is a low-angle boundary formed by closely spaced edge-type dislocations. Details of high-resolution X-ray topography experiments on all specimens carried out by using different reflections will be published separately.

The results of the foregoing experiments have shown that the degree of perfection of our specimens varies considerably. We selected specimens with different degrees of crystalline perfection for the study of point defects and their clusters by diffuse X-ray scattering measurements.

3.3. Characterization of point defect clusters in diamond specimens by using high-resolution diffuse X-ray scattering (DXS) measurements

High-resolution diffuse X-ray scattering (DXS) measurements have been made in Bragg geometry on specimens having different degrees of crystalline perfection. In each specimen crystal, the region to be explored was selected carefully to ensure that a single well defined peak was observed in its diffraction curve. Stationary topographs were also recorded and the value of ρ was determined before DXS measurements.

First of all, we shall describe the results of diffuse X-ray scattering measurements made on specimen 13, which was found to have the highest degree of perfection (§3.2, Figs. 3, 5 and 6). Fig. 7 shows a typical set of log DXS(I) vs log K^* plots for this specimen. Here, **K*** is
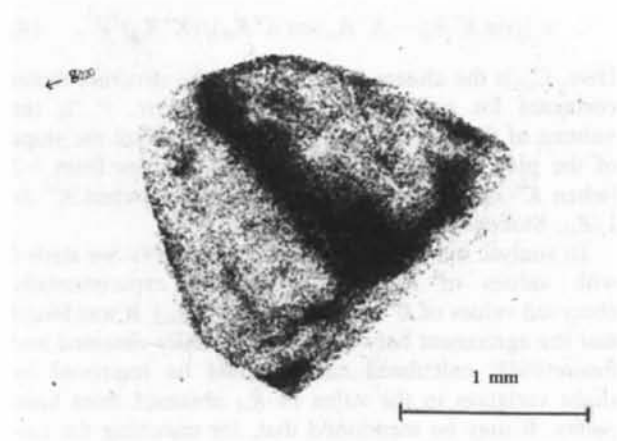

Fig. 5. A typical high-resolution X-ray traverse topograph of diamond specimen 13 recorded with $(\bar{2}20)$ diffracting planes in symmetrical Laue geometry. Mo $K\alpha_1$ radiation and $(+, -, +)$ configuration of the diffractometer were employed.
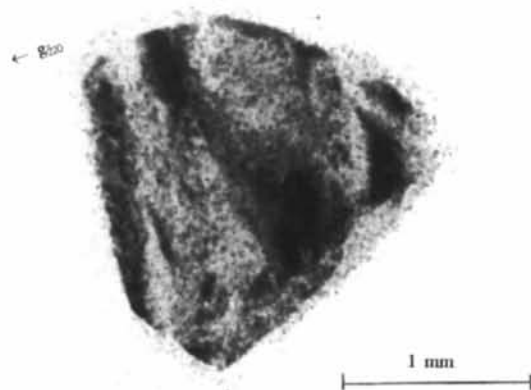

Fig. 6. A set of high-resolution stationary X-ray topographs of the diamond specimen 13 recorded with $(\bar{2}20)$ diffracting planes in Laue geometry. The specimen and the film were translated across the X-ray beam by a linear distance equal to the width of a stationary topograph and the entire volume of the specimen was covered. Other experimental details are identical to those of Fig. 5.

the vector that joins the elemental volume under investigation to the 111 reciprocal-lattice point (r.l.p.) around which DXS measurements were made. The DXS measurements were made along four directions of $\mathbf{K}^*$ in the reciprocal space, namely [111], [$\bar{1}\bar{1}\bar{1}$], [1$\bar{1}$0] and [$\bar{1}$10] around 111 r.l.p. At each $\mathbf{K}^*$ value, the magnitude of the observed DXS intensity was quite large compared with the theoretically expected Bragg diffracted intensity from an ideally perfect crystal and hence no correction was made for the contribution from dynamical diffraction. It is seen from the figure that, for any value of $\mathbf{K}^*$, the value of the DXS intensity is not the same along all directions. For any value of $\mathbf{K}^*$, it is higher for $\mathbf{K}^*$ parallel to reciprocal-lattice vector $\mathbf{R}^*$ compared with the value for $\mathbf{K}^*$ perpendicular to $\mathbf{R}^*$. From this observation, one can conclude that at room temperature the observed DXS is predominantly due to the point defect aggregates rather than the phonons as shown earlier by Lal and co-workers for other crystals (Lal *et al.*, 1979; Lal, 1989).

For any direction of $\mathbf{K}^*$, the DXS plot is not a single straight line but consists of more than one segment with different slopes. Further, it is seen that there is an anisotropy in the distribution of DXS intensity with respect to the sense of $\mathbf{K}^*$. The scattered intensity is higher for $\mathbf{K}^*$ along [$\bar{1}\bar{1}\bar{1}$] compared with that for $\mathbf{K}^*$ along [111]. Such an anisotropy in the DXS distribution is expected from defects (Dederichs, 1973). In this case, the observed anisotropy is negative (*i.e.* $I_{\theta>\theta_b} < I_{\theta<\theta_b}$) for all directions of $\mathbf{K}^*$. Such a negative anisotropy shows that the vacancy type of defects gives dominant contribution to the diffuse scattering (Lal, 1989; Ramanan *et al.*, 1995).
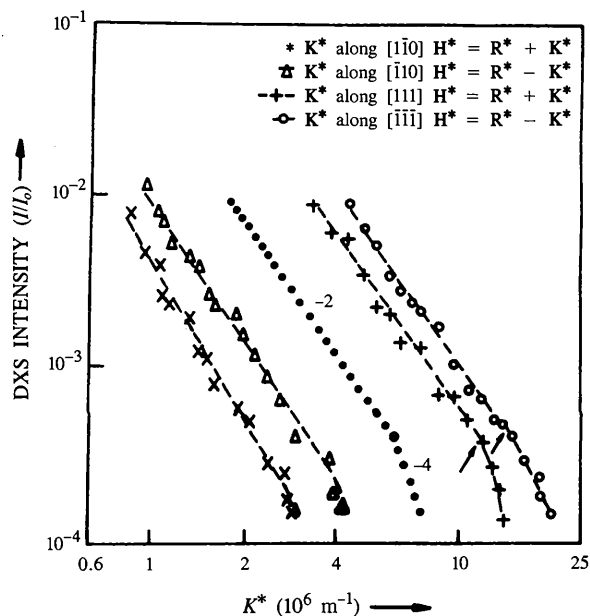
It is seen from Fig. 7 that, at lower values of $\mathbf{K}^*$, the plot is almost a straight line with a slope of ~−2. At higher values of $\mathbf{K}^*$, line segments with slope ~−4 are also seen. For $\mathbf{K}^*$ along ⟨110⟩, the curves follow a −2 slope [Huang scattering region (Huang, 1947)] for the value of $\mathbf{K}^*$ in the range 6×10^5 to 3×10^6 m^{-1}. For $\mathbf{K}^*$ greater than 3×10^6 m^{-1}, a tendency towards greater slope can be seen. However, as the DXS intensity falls below 0.5 counts s^{-1}, only a few points are shown. For $\mathbf{K}^*$ along ⟨111⟩, one can clearly see line segments with two slopes. The knee points (K_{knee}), where the slope changes from ~−2 to ~−4 are shown by arrows. The region with slope −2 is attributed to isolated point defects (Huang scattering) and that with slope −4 is due to clusters of point defects [Stokes–Wilson scattering region (Stokes & Wilson, 1944)]. For convenience of comparison, dotted lines with slopes equal to −2 and −4 are also shown in Fig. 7. One can estimate the approximate size of the cluster from the value of K^*_{knee} ($K_{knee} = 1/R_{cl}$) (Lal, 1989). In the present case, the knee points are at K^* values 1.2×10^7 and 1.6×10^7 m^{-1}, which yield two sizes: ~8×10^{-8} and ~6×10^{-8} m.

Theoretical calculations of diffusely scattered X-ray intensities from crystals containing isolated point defects as well as clusters have been made by several authors (Dederichs, 1973; Larson & Schmatz, 1980). These are basically model calculations and simplifying assumptions are made to bring the problem within the solvable range. We have used one such phenomenological model worked out for the case of dislocation loops which is applicable for small concentration of defects (Dederichs, 1973). According to this, the intensity of the diffusely scattered X-rays, $S(\mathbf{R}^* + \mathbf{K}^*)$ is given by

$$S(\mathbf{R}^* + \mathbf{K}^*)$$
$$= C_{cl}|F_{pT}|^2| - 4\pi(A_{cl}/V_c)[(\mathbf{R}^* \cdot \mathbf{K}^*)/K^{*2}]$$
$$\times [(\sin K^* R_{cl})/K^* R_{cl}] - (4\pi R_{cl}^3/V_c)$$
$$\times [(\sin K^* R_{cl} - K^* R_{cl} \cos K^* R_{cl})/(K^* R_{cl})^3]|^2. \quad (4)$$

Here, C_{cl} is the cluster density, F_{pT} is the structure factor corrected for polarization and temperature, V_c is the volume of the unit cell and $A_{cl} = R_{cl}^2/R^*$. Here the slope of the plot between DXS(I) and K^* changes from −2 (when $K^* \ll 1/R_{cl}$; Huang region) to −4 (when $K^* \gg 1/R_{cl}$; Stokes–Wilson region).

To analyse our experimental data using (4), we started with values of R_{cl} calculated from experimentally observed values of K^* at knee points ($1/R_{cl}$). It was found that the agreement between experimentally obtained and theoretically calculated curves could be improved by slight variation in the value of R_{cl} obtained from knee points. It may be mentioned that, for matching the calculated and observed intensities, a suitable scaling factor depending on the resolution factor defining the experimental conditions was used. In this particular crystal, keeping in view the presence of the vacancy type of

Fig. 7. A typical set of log DXS(I) vs log K^* plots for the diamond specimen 13. Mo $K\alpha_1$ radiation, 111 r.l.p. and (+, −, −, +) geometry of the diffractometer were used.

defect clusters, the theoretically expected distribution with K^*along [$\bar{1}\bar{1}\bar{1}$] has been computed. Fig. 8 shows the experimental data points and the theoretically computed curve (full lines). A reasonably good agreement is seen between the two for an R_{cl} value of 5.4×10^{-8} m. The other cluster parameters obtained by using this value of R_{cl} are cluster volume $(A_{cl}) = 1.8 \times 10^{-25}$ m^3 and number of defects per cluster $(N_{cl}) = 3.9 \times 10^3$.

DXS measurements were also made on a specimen crystal (specimen 4) with degree of perfection lower than that of specimen 13 whose results are reported above. The half-width of its diffraction curve was ~24″ and the value of ρ was determined as 4×10^{-5} rad. X-ray diffraction topography results also supported the above observation. Fig. 9 shows a typical DXS(I) vs K^* plot (on a log–log scale) for this specimen. In this case, the general features of the plot are the same as those for specimen 13 except for some important differences. DXS measurements made along ⟨111⟩ clearly showed a positive anisotropy indicating that the defects responsible for scattering were interstitials in nature. The plots show a −2 slope at lower K^* values and −4 slope at higher K^* values along ⟨111⟩. From the knee points K^*_{knee} (shown by arrows), the cluster radii were determined to be 1.3×10^{-7} and 2×10^{-7} m. For K^* along ⟨110⟩ and the value of K^* in the range 6×10^5–3×10^6 m^{-1}, the curves have a slope of ~−2 at lower values of K^*. The extreme points show a tendency towards a higher slope, as seen in the case of specimen 13. The magnitude of anisotropy for this direction of K^* was very small. However, a detailed analysis showed it to be positive.

Keeping in view the interstitial nature of defect clusters, the theoretically expected DXS intensity distribution was computed for K^* along [111] using the model calculations of (4). A good match between the experimental data points and the theoretical plot was obtained for $R_{cl} = 1.9 \times 10^{-7}$ m. Fig. 9 shows both the experimentally obtained data points and theoretically computed curve (full line). The other defect parameters calculated for this specimen were $A_{cl} = 28 \times 10^{-25}$ m^3 and $N_{cl} = 62 \times 10^3$.

DXS measurements were also made on specimen 1 whose diffraction curve was quite broad with the value of the half-width ~35″. Also, the value of ρ $(5.8 \times 10^{-5}$ rad) was found to be higher than those of other specimens whose results are reported above. However, the diffraction curve was well defined and the stationary topograph did not reveal any individual dislocations. From the analysis of experimental data and the theoretical model, it was found that the interstitial defect clusters are predominantly responsible for the observed DXS intensity. The defect parameters obtained by applying the model of (4) were $R_{cl} = 4.1 \times 10^{-8}$ m, $A_{cl} = 1.1 \times 10^{-25}$ m^{-3} and $N_{cl} = 2.5 \times 10^3$. The values of defect parameters calculated for all the investigated specimen crystals are given in Table 2.

Experiments were performed with a highly imperfect crystal (No. 3) whose diffraction curve half-width was 550″ with $\rho = 75 \times 10^{-5}$ rad. Fig. 10 shows a typical log DXS(I) vs log K^* plot for the specimen. Here, one can see regions with slope −4, indicating the presence of clusters. At higher K^* values (i.e. $K^* > 5 \times 10^7$ m^{-1}), segments with slope higher than −4 are also seen. This is
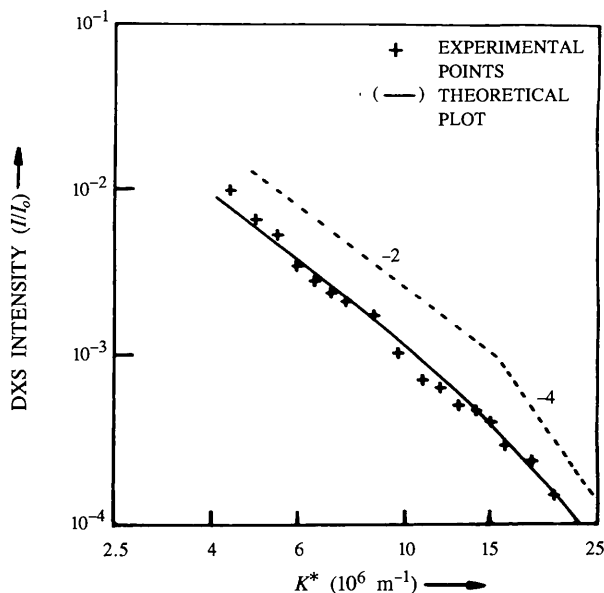

Fig. 8. Theoretically calculated DXS(I) vs log K^* plot (solid line) for diamond specimen 13 for K^* along [$\bar{1}\bar{1}\bar{1}$]. The experimentally obtained data points are shown by +. Dotted lines with slopes −2 and −4 are also shown for convenience of comparison.
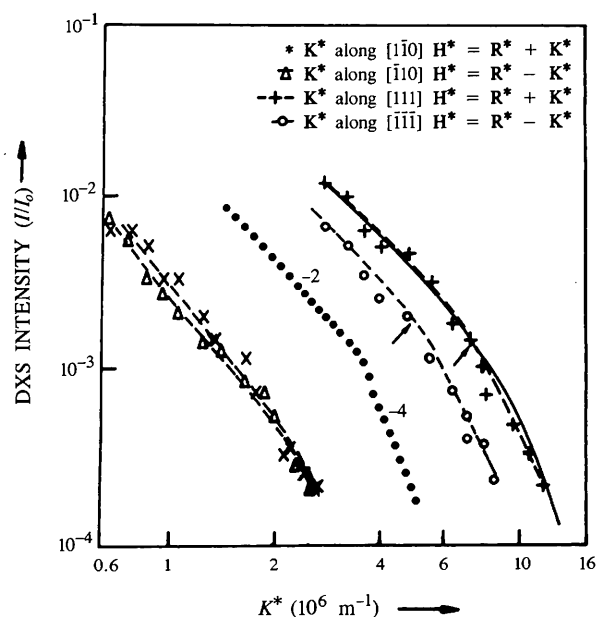

Fig. 9. Typical log DXS(I) vs log K^* plots for the diamond specimen 4. Theoretically calculated DXS(I) for K^* along [111] is shown by the solid line.

Table 2. *Type of defect cluster and values of cluster radius (R_{cl}), volume of cluster (A_{cl}) and number of defects per cluster (N_{cl}) in various samples*

Sample	Type of defects	R_{cl} ($\times 10^{-9}$ m)	A_{cl} ($\times 10^{-25}$ m^3)	N_{cl} ($\times 10^3$)
No. 1	Interstitial aggregates	41	1.1	2.5
No. 3	–	60	–	–
No. 4	Interstitial aggregates	190	28	62
No. 13	Vacancy aggregates	54	1.8	3.9

again an expected feature for defect clusters (Dederichs, 1973; Lal, 1989). The presence of unresolved peaks in the diffraction peak made it difficult to determine the sign of anisotropy. Also, the model calculation could not be applied. However, from the knee points, the approximate value of cluster size was determined to be ~6 × 10^{-8} m.

Defects in diamond crystals have been investigated by a number of experimental techniques like X-ray diffraction topography, cathodoluminesense topography, birefringence microscopy, electron energy-loss spectroscopy (EELS) and TEM. These studies have revealed the internal growth features, dislocation features, stacking faults, voidites and platelet defects (Lang et al., 1992; Barry et al., 1987, Bruley & Brown, 1989; Jiang et al., 1987). Most of the X-ray topographic works have been reported by Lang and co-workers. They employed a variety of topographic techniques like projection, limited projection, section topography and 'spike' topography in their studies (Lang, 1974; Lang et al., 1985). Lang et al. (1985) observed spike diffuse reflections while employ-
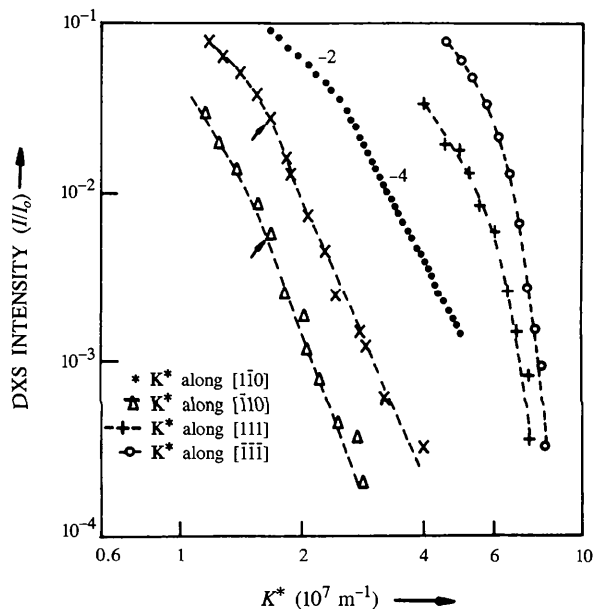

Fig. 10. Typical log DXS(I) vs log K^* plots for the diamond specimen 3. Dotted lines with slopes −2 and −4 are also shown for convenience of comparison.

ing continuous synchrotron radiation and interpreted them as being due to 'voidites' (with diameter ~1 nm) in type Ia diamonds. Clackson et al. (1990) have employed spike topography and infrared and TEM techniques to measure the sizes of the platelets. Using spike topography, they observed platelets of sizes 10–25 nm in their samples. This work was primarily aimed at finding the relationship between the platelet size and the frequency of the platelet IR absorption peak. The defect sizes reported by Lang et al. (1985) and Clackson et al. (1990) are considerably smaller than those reported in the present work. The difference primarily arises due to our leaving out that volume of reciprocal space that would have given information about the defect clusters of sizes of ~20 nm or less. The observed DXS intensity for this region of reciprocal space was too small for measurements with a reasonable level of uncertainity. However, it should be noted that the reciprocal space so close to the r.l.p.s has been explored for the first time. Therefore, results for defects reported here have considerable significance. Fuji et al. (1995) have employed double-crystal X-ray diffraction and positron annihilation techniques and have indicated the presence of vacancy types of defect clusters in their samples.

Results obtained by TEM measurements by various investigators have also revealed platelets and dislocation loops of both vacancy and interstitial nature in natural diamond crystals (Evans & Phall, 1963; Barry et al., 1987). Platelets with dimensions from nanometre size to several micrometres have been observed by this technique. Woods (1976) reported perfect dislocation loops of interstitial character on {100} planes. He had reported 'giant' platelets of size up to 5 μm. However, this technique is destructive and demands tedious sample preparation processes.

The results reported here have shown that there is a significant amount of nitrogen in A and B forms and the platelet form in the investigated diamond specimens. While the amount of nitrogen in the A defect form varies from ~60 to ~600 atoms in 10^6, in the B defect form it varies from ~100 to ~500 atoms in 10^6. Also, there is a considerable variation in platelet defect concentration from sample to sample. The high-resolution X-ray diffraction experiments revealed a large variation in the degree of perfection of diamond samples. Even within each crystal, variation in perfection has been observed. This is not very surprising considering the origin of the diamond crystals (Davies, 1994). Optical, birefringence and topographic studies (Evans, 1976) of diamond crystals have shown that natural diamonds exhibit a variety of defects. High-resolution DXS measurements have revealed that in the investigated samples the point defects have aggregated into clusters of sizes 40 to 190 nm of either vacancy or interstitial types with cluster volume 1 × 10^{-25} to 28 × 10^{-25} m^3.

In the case of sample 1, the diffraction curve was well defined and the topographs did not reveal any dislocation

features. However, the value of ρ was quite large. This could be due to the presence of a high concentration of platelet defects. This is evident from the large value of μ (22 cm^{-1}) in the IR spectra. In fact, this is the largest value of μ observed in this investigation. The DXS measurements reveal that the defects are predominantly interstitial in nature with cluster size ~40 nm. From this, one can conclude that the clusters are more like small platelet-like defects. In the case of sample 4, the diffraction curve is sharper than that of sample 1 and the magnitude of ρ is also lower. The DXS measurements show that the defects are interstitial in nature, but of larger size platelets (190 nm). However, the platelet band is much weaker ($\mu = 2.4$ cm^{-1}) as compared with that of sample 1. From this result, we can conclude that the concentration of platelets is much lower in this sample in comparison with specimen 1. If one considers the total amount of nitrogen in A and B aggregate forms of nitrogen in samples 1 and 4, the amount of nitrogen in sample 1 is higher compared with that of sample 4, whereas the platelet size is smaller in the former than in the latter. A similar result was reported by Clackson et al. (1990). In the case of sample 13, which shows the sharpest diffraction curve of all (Fig. 3), the clusters are predominantly of vacancy type with cluster size ~54 nm. In this case, the magnitudes of ρ and the platelet concentration are also quite low. From this, one can conclude that the defect clusters are more like dislocation loops formed by vacancies. Such a condensation of vacancies resulting in dislocation loops has been reported by Evans & Phall (1963). They had observed dislocation loops of vacancy type on {111} planes of type Ia diamonds. They reported long thin loops of length 200 to 700 nm in their specimens with a defect concentration up to 4×10^{25} vacancies m^{-3}. Sample 3 exhibited the weakest platelet peak of all. However, it had the broadest diffraction curve of all with largest value of ρ. This can be understood in terms of unresolved low-angle boundaries in the crystal.

The results reported have shown that the high-resolution DXS technique together with diffractometry and topography is quite useful for the characterization of platelet defects and dislocation loops in natural diamonds.

References

Barry, J. C., Bursill, L. A., Hutchison, J. L., Lang, A. R., Rackham, G. M. & Sumida, N. (1987). *Philos. Trans. R. Soc. London*, **321**, 361–401.

Bonse, U. & Hart, M. (1965). *Appl. Phys. Lett.* **7**, 238–240.

Bruley, J. & Brown, L. M. (1989). *Philos. Mag.* A**59**, 247–261.

Clackson, S. G., Moore, M., Walmsley, J. C. & Woods, G. S. (1990). *Philos. Mag.* B**62**, 115–128.

Davies, G. (1981). *Nature (London)*, **290**, 40–41.

Davies, G. (1984). *Diamond.* London: Adam Hilger.

Davies, G. (1994). *Mater. Sci. Forum*, **143**, 21–28.

Dederichs, P. H. (1973). *J. Phys. F*, **3**, 471–496.

Evans, T. (1976). *Contemp. Phys.* **17**, 45–70.

Evans, T. & Phall, C. (1963). *Proc. R. Soc. London Ser. A*, **270**, 538–552.

Field, J. E. (1992). *Properties of Natural and Synthetic Diamond.* London: Academic Press.

Fuji, S., Nishiyabayashi, Y., Shikata, S., Uedono, A. & Tanigawa, S. (1995). *J. Appl. Phys.* **78**, 1510–1513.

Holy, V. & Kubena, J. (1992). *Phys. Status Solidi B*, **170**, 9–25.

Huang, K. (1947). *Proc. R. Soc. London Ser. A*, **190**, 102–117.

James, R. W. (1950). *Optical Principles of the Diffraction of X-rays.* London: Bell.

Jiang, S. S., Lang, A. R. & Tanner, B. K. (1987). *Philos. Mag.* A**56**, 367–375.

Kiflawi, I., Mayer, A. E., Spear, P. M., Van Wyk, J. A. & Woods, G. S. (1994). *Philos. Mag.* B**69**, 1141–1147.

Lal, K. (1989). *Prog. Cryst. Growth Charact.* **18**, 227–266.

Lal, K. (1993). *Bull. Mater. Sci.* **16**, 617–642.

Lal, K. & Bhagavannarayana, G. (1989). *J. Appl. Cryst.* **22**, 209–215.

Lal, K., Goswami, S. N. N. & Verma, A. R. (1990). *Pramana J. Phys.* **34**, 507–523.

Lal, K., Goswami, S. N. N. & Verma, A. R. (1995). *Solid State Commun.* **96**, 33–36.

Lal, K., Singh, B. P. & Verma, A. R. (1979). *Acta Cryst.* A**35**, 286–295.

Lang, A. R. (1974). *J. Cryst. Growth*, **24/25**, 108–115.

Lang, A. R., Kowalski, G., Makepeace, A. P. W. & Moore, M. (1985). *Philos. Mag.* A**52**, L1-L6.

Lang, A. R., Moore, M. & Walmsley, J. C. (1992). *Properties of Natural and Synthetic Diamond*, edited by J. E. Field, pp. 215–258. London: Academic Press.

Larson, B. C. & Schmatz, W. (1980). *Phys. Status Solidi B*, **99**, 267–275.

Ramanan, R. R., Bhagavannarayana, G. & Lal, K. (1995). *J. Cryst. Growth*, **156**, 377–382.

Ramanan, R. R. & Lal, K. (1996). *Acta Cryst.* A**52**, C522.

Stokes, A. R. & Wilson, A. J. C. (1944). *Proc. R. Soc. London*, **56**, 174–181.

Walker, J. (1979). *Rep. Prog. Phys.* **42**, 1605–1659.

Woods, G. S. (1976). *Philos. Mag.* **34**, 993–1012.

Woods, G. S., Purser, G. C., Mtimkulu, A. S. S. & Collins, A. T. (1990). *J. Phys. Chem. Solids*, **51**, 1191–1197.